

Modeling and Experimental validation of Nickel-based super alloy (Inconel 625) made using Selective Laser Melting

Md Ashabul Anam, Deepankar Pal, Brent Stucker
Department of Industrial Engineering,
J. B. Speed School of Engineering, University of Louisville, Louisville, KY 40292

Abstract

The formation of constituent phases in Selective Laser Melting of Inconel 625 is a function of local temperatures, hold times at those temperatures, local cooling rates and local compositions in the melt pool. These variables are directly correlated with input process parameters such as beam power, scan speed, hatch spacing, beam diameter and thermo-mechanical characteristics of the powder bed. The effect of these process parameters must be understood in order to properly control the machines and predict the properties of parts being fabricated. To understand the effects, IN625 coupons using eight different sets of processing parameters have been fabricated and microstructure and mechanical properties were compared. These properties will be then used to validate a dislocation density based crystal plasticity finite element model (DDCP-FEM).

Introduction:

Inconel 625, a nickel based super alloy is characterized by having high tensile, creep and rupture strength and is widely used because of its excellent fatigue and good oxidation resistance properties. However, excessive tool wear and low material removal rate make it difficult to manufacture by conventional machining methods at room temperature. Selective laser melting (SLM) therefore becomes a good solution for complex IN625 parts. SLM involves directional solidification concepts as well as novel prospects for microstructure control through the development of scanning strategies or related process variables such as local temperature, hold time at temperature, local cooling rate and local compositions in the melt-pool. These features produce solidification cooling rate and thermal gradient phenomena which contribute to microstructure and microstructural architecture development and resulting mechanical properties [1-2]. The effect of each process parameter on the resulting microstructure and mechanical properties must be understood in order to properly control the machines and predict the properties of the parts being fabricated.

To predict the mesoscopic effect such as local and global strength, modified grain morphologies and other layer by layer interfacial characteristics on the end part, a homogenized form of the Dislocation Density based Crystal Plasticity Finite Element Model (DDCP-FEM) will be used. Information from an IN625 CCT diagram along with build part geometry information from the STL file and thermo-mechanical boundary conditions of the SLM process will be used as input parameters to the model.

To validate the model a series of experiments on IN625 with SLM need to be performed. These experiments include IN625 powder characterization, parameter optimization for successful coupon fabrication, capturing temperature distributions near the molten pool, microstructural characterization and mechanical testing. Mechanical test and microstructural results will be used to create a structure-property correlation which will be matched with the model.

Materials and experimental procedures

IN625 powder characterization:

In this experiment IN625 powders from EOS have been used. Analysis has been done on the powder and necessary information gathered to inform the model, including physical and chemical properties, particle size distribution and density. Chemical composition is shown in table 1. This composition was verified through EDS analysis. To obtain the particle size distribution, a Microtrac S3000 particle size analyzer was used. The mean diameter of the particles is 37.8 microns (mean dia. of volume dist.) with a standard deviation of 12.37 microns, 70 percent of the particles below 40 microns which indicates particles are distributed within a narrow size range and are suitable for SLM processing. Figure 1 shows the morphology of IN625 powder which was captured using scanning electron microscopy (FEI Nova Nano SEM). Both 20 and 40 micron layer thickness have been used to check optimality. Table 3 shows the powder density measurements which are critical parameter to know as they influence flowability. The bulk density was found to be 4.351 gm/cc where the tapped density was 5.072 gm/cc. The Hausner ratio and Carr's index were also calculated to determine the flow properties of the powder. The Hausner ratio was 1.166 (< 1.25 indicates that the powder is free flowing). The Carr's index was 14.216 which indicates that the powder has good flow properties.

Table 1: Chemical Composition (Wt.%) of IN625 powder

Ni	Cr	Mo	Nb	Fe	Ti	Al	Co	C	Ta	Si,Mn	P,S
bal. \geq 58.00	20.00- 23.00	8.00- 10.00	3.15- 4.15	\leq 5.00	\leq 0.40	\leq 0.40	\leq 1.00	\leq 0.10	\leq 0.05	each \leq 0.50	each \leq 0.015

*Obtained from EOS material data sheet

Table 2: Particle Size Analysis:

Instrument: Microtrac S3000

Summary	Value	Unit
Mean Dia. of the Volume distribution *	37.78	μm
Mean Dia. of the Number distribution **	20.05	μm
Mean Dia. of the Area distribution †	31.8	μm
Calculated Specific Surface Area, CS ⁺⁺	1.89E-01	M ² /CC
Standard Deviation, SD	12.37	μm

Table 3: Density measurement:

Material	In625 powder
Bulk density , ρ_B	4.351 gm/cc
Tapped density , ρ_T	5.072 gm/cc
Hausner Ratio, H, (ρ_T/ρ_B)	1.166
Carr Index, C	14.216

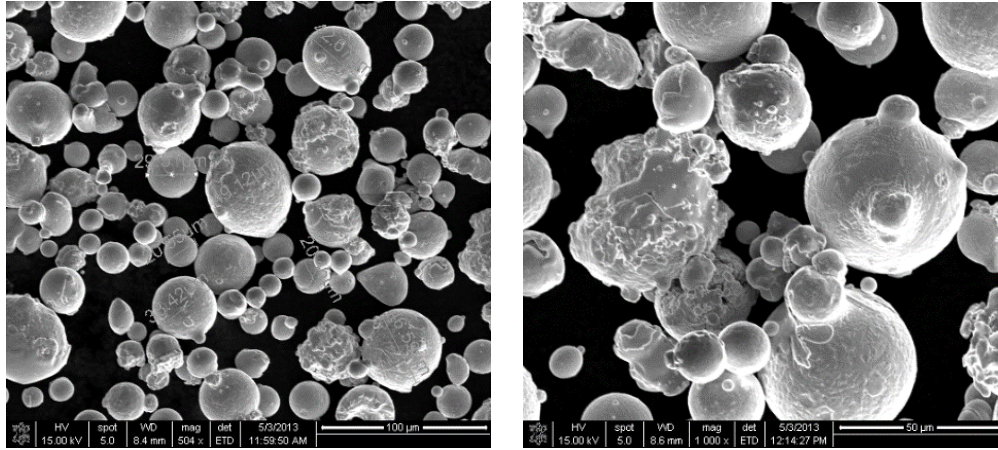


Figure1. SEM image of IN625 powder

Test coupon fabrication with varying processing parameters:

IN625 test coupons of 5*5*5 mm³ were fabricated using an EOS M270 DMLS machine in nitrogen atmosphere. Different processing conditions such as scan speed, laser power and scan strategy have been used to experimentally characterize variance in microstructural and mechanical behavior. Two sets of parameters defined by constant energy density and varying energy density were used. Each set contains 4 subsets of parameters of varying laser power and/or scan speed. Parameter sets are shown in Table 4. Tensile and fatigue bars were also fabricated for mechanical testing and validation. Both 20 and 40 micron layer thicknesses were used to build the coupons and the density of as-built parts were compared.

Table 4: Processing parameters of IN625 for an EOS M270 machine:

Parameter set		Subset	Laser Power (W)	Scan Speed (mm/s)	Spacing (mm)
1	Constant Energy Density	1	195	800	0.1
		2	170	697	0.1
		3	145	594	0.1
		4	120	492	0.1
2	Constant Laser power, Varying Energy Density	1	195	1100	0.1
		2	195	1000	0.1
		3	195	900	0.1
		4	195	700	0.1

Density measurement technique:

Density was measured using an Archimedes method. Masses of each coupon in air and water were measured independently 3 times using an electronic balance with $\pm 1\text{mg}$ accuracy. Similarly, average masses were calculated by taking means of masses in air and water for each coupon and denoted using m_a and m_w respectively. The average masses were inserted into the equation below to obtain coupon density ρ_p , where ρ_w is the density of water [6]. Temperature correction was applied for calculating ρ_w .

$$\rho_p = \frac{m_a}{m_a - m_w} \times \rho_w$$

Microstructural characterization:

As-built parts were processed for microstructural characterization. Standard metallographic specimen preparation methods were followed during specimen preparation. Polished samples were electrolytically etched for approx. 10 sec. in 7.5 % Oxalic acid solution. Microstructures of vertical cross sections (Y-Z plane) of 16 samples (8 samples each of 20 and 40 micron layer thickness) were observed using optical microscopy. Melt-pool overlap, variation and grain size were the points of interest in the microstructural analysis.

Results and Discussion:

Comparison of density of parts made using 20 and 40 micron layer thickness:

To identify the layer thickness effect, test coupons built using 20 and 40 micron layer thickness were compared. This comparison was based on as-built part density for coupons fabricated using 195W laser power and 800 mm/s scan speed. Figure 2 below shows the density comparison between samples of 20 and 40 micron layer thickness.

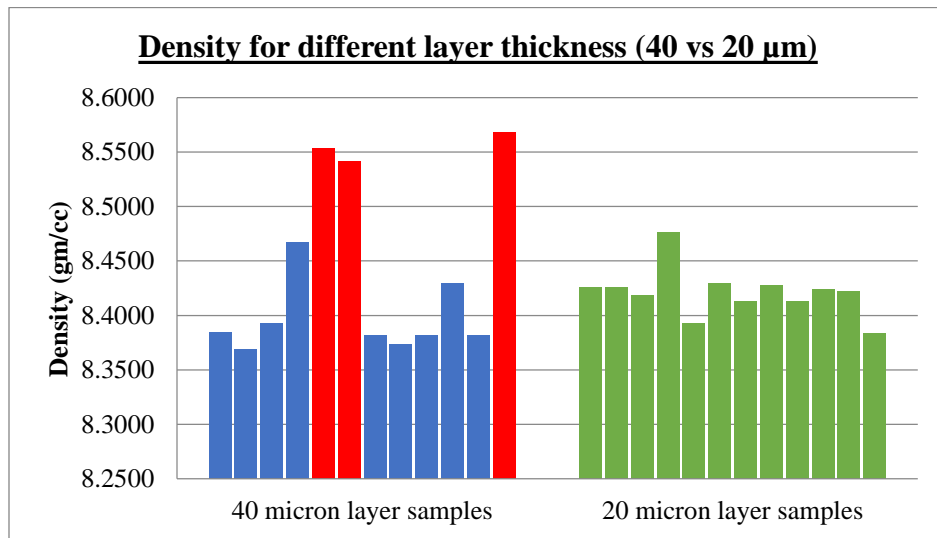


Figure 2: Density of coupons manufactured using 20 and 40 micron layer thickness with laser power 195W and scan speed 800mm/s

From the above figure it can be seen that there is a high variability in density of 40 micron layer samples where for 20 micron the density data are quite consistent. Based on this initial screening study, a decision cannot be made on which layer thickness provides higher density. If the three 40 micron outlier data points (marked as red bar) are excluded, however, parts made using 20 μm layer thickness have a consistently higher density than 40 μm layer parts. Thus, further studies are required to determine whether experimental error led to these outlier data points and whether there is indeed a large scatter in density. One reason to question these results is that fully dense IN625 parts have a theoretical density of 8.44 gm/cc [7], which is close to the density of 20 micron SLM parts, giving a theoretical average 8.42 gm/cc, or 99.76%, density.

Image Analysis – Variation of Melt-pool:

Distribution of melt pool has been analyzed using optical microscopy Figure 3.a. shows micrographs of vertical cross-sections (Y-Z plane) of samples with 20 micron layer thickness where figure 3.b. shows the same micrograph produced by 40 micron layer thickness. Laser power was 195W and scan speed was 800 mm/s in both cases.



Figure 3.a. Vertical cross-section for layer thickness 20 micron, Laser Power 800W, Scan speed 800mm/s.



Figure 3.b. Vertical cross-section for layer thickness of 40 micron, Laser Power 800W, Scan speed 800mm/s.

It is quite clear from the above micrographs that the patterns of melt-pools of 40 μm layers are different from 20 μm layers. For 20 μm , melt pools are regular in shape and overlap each other significantly whereas for 40 μm , melt pool shape is irregular and are less overlapped. 20 μm layer thickness parts would be expected to have a higher density and better mechanical properties than 40 μm layer parts as a result. Fatigue and tensile test bars were manufactured to compare mechanical properties. In addition, melt-pool comparisons were done for other 20 and 40 micron layer thickness coupons for the other 7 processing parameters and in general there was better melt-pool distribution and overlap for 20 micron than 40 micron layer thickness coupons. Melt-pool overlap was calculated through image analysis for all eight processing parameters and a comparison is shown in figure 4.

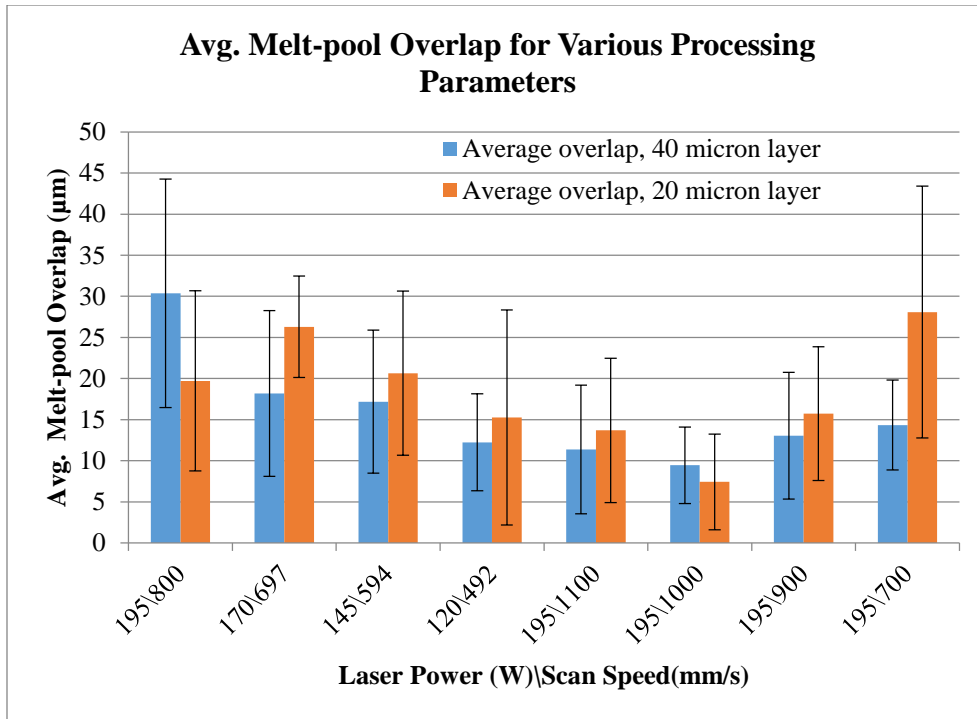


Figure 4: Average melt-pool overlap in test samples in Z-direction.

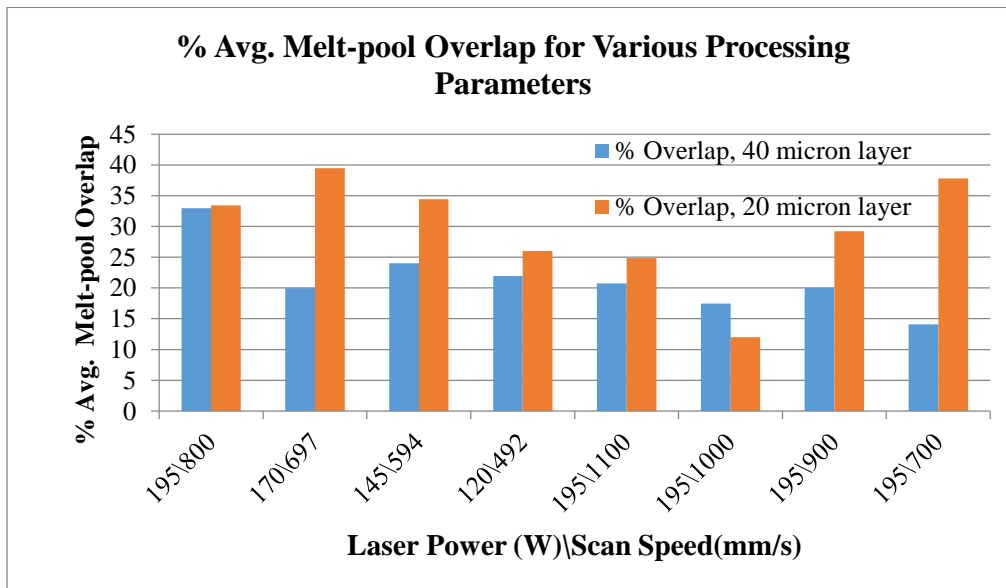


Figure 5: % Average melt-pool overlap in test samples.

Figure 4 above, shows avg. melt-pool overlap in build direction (Z-axis). It is distinguishable that most of the processing parameters with 20 micron layer thickness have higher melt-pool overlap than 40 micron except the first one (195W,800 mm/s) but from figure 5, for the same parameter set (195W, 800mm/s), a higher percentage of melt-pool overlap was found for 20 micron than 40 micron layer thickness. The difference between figure 4 and figure 5 arise due to

uneven melt-pool size. For example, a 30 micron overlap can cast different percentage overlap value depending on overall melt-pool depth.

Figure 4 also shows a gradual decrease in overlap as the laser power and scan speed decrease. Also at high power (195 W) and high scan speed (1000 mm/s) overlap was less. This is due to excessively high scan speed. The sample prepared using this parameter is expected to have lower density and less tensile and fatigue strength. Although at constant laser power (195W), melt-pool overlap increased with the decrease of scan speed. From the melt-pool data it can be inferred that 195W/800mm/s, 195W/700mm/s and 170w/697mm/s, associated with 20 micron layer thickness, are the three parameter sets which provide highly dense parts with higher melt-pool overlap. Figure 6 (a,b,c) shows verticle cross-sections of these 3 parameter sets. As the variability is high in melt-pool overlap data in figure 4, it is obvious that more experimental data is required before drawing a conclusion based on overlap data. Also mechanical testing (fatigure, tensile) need finished to support any conclusions.



Fig. 6 (a,b,c) LOM image of vertical section of 20 micron layer thickness of (a) 190W/800mm/s, (b) 170W/697mm/s, (c) 190W/700mm/s

Mechanical testing and validation:

Near-net shape specimens have been fabricated for tensile and fatigue studies. Tensile tests will be performed as per ASTM E 8M and high cycle fatigue tests will be performed as per ASTM E466. Mechanical test results and microstructural results will be used to create a structure-property correlation which will be matched with the model. Figure 7 shows fatigue bars built in horizontal and vertical orientations.



Figure 7: IN625 Hi-cycle Fatigue bars fabricated in vertical and horizontal orientations.

Microstructural characterization:

In figure 8, melt banding is easily distinguished due to its dark contrast. The dark contrast arises from a large amount of γ'' (bct-Ni₃Nb) precipitates. This same type of precipitate was also reported in the work of Amato et al, 2012 [2]. Fine dendritic structures can also be seen in figure 8, which are due to columnar precipitates. The fine dendritic structures indicate high cooling rate in the negative Z direction.

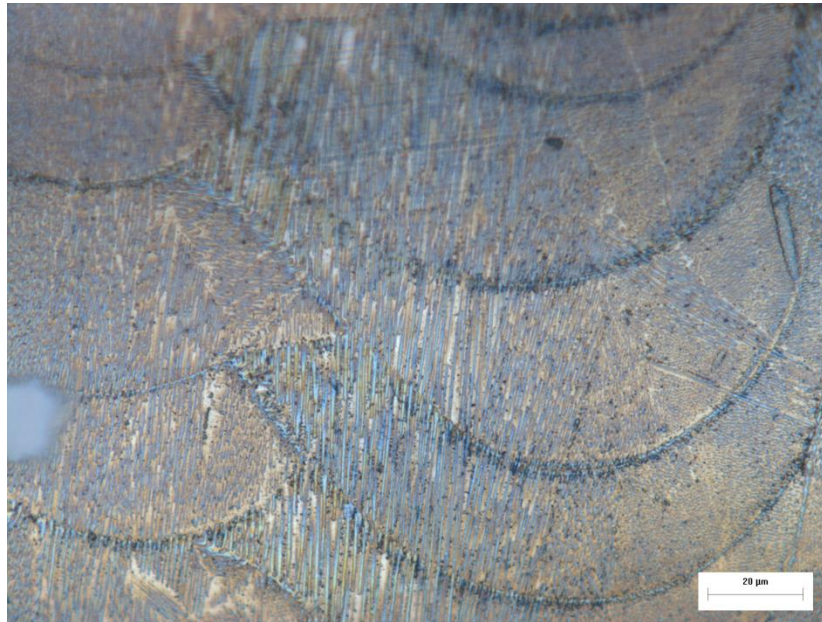


Figure 8: Micrograph showing γ'' secondary precipitation morphology. IN625 image of a vertical cross-section (195W laser power, 800 mm/s scan speed, 20 μm layer thickness).

Future work:

Validation of finite element model:

To predict the properties of the parts being fabricated a finite element model will be used. An accurate model must predict the effects of two temperature regimes: (1) rapid heating by a laser to a fully molten, elevated temperature; and (2) rapid cooling of the melt pool. In order to capture the physics of these temperature regimes and properly predict the effects of various process parameters on the end part, several modeling tools will be used. The sensitivity of the constituent phases with respect to the temperature and time at temperature can be interpreted from Continuous Cooling Transformation (CCT) diagrams. These CCT diagrams can be theoretically computed using the CALculation of PHase Diagrams (CALPHAD) [10] software. The computed CCT diagrams can be used for prediction of equilibrium and metastable phases/grain morphologies as a function of location in the build, temperature, time at temperature, and cooling rate(s). This information, coupled with the build part geometry information from the STL file

and thermo-mechanical boundary conditions of the DMLS process, will be used as input parameters for a homogenized form of the Dislocation Density based Crystal Plasticity Finite Element Model (DDCP-FEM) [11-16] to predict mesoscopic effects such as local and global strengths, modified grain morphologies, and dislocation densities.

Extraction of heat flux at molten pool boundary:

The temperature distribution at the molten pool boundary during solidification is a key to effective modeling of DMLS. Experimentally a FLIR thermal camera recording at 200 frames per second (fps) and resolution of 25 microns will be utilized. Similar work was reported by Rodriguez et al. for EBM processing [17]. Analytically, best practices will be used to estimate the heat flux based upon known models and solutions in the literature. Numerically, the experimental and analytical information will be integrated into a finite element model to predict the heat flux boundary conditions in a dynamic manner based upon process parameter inputs. The temperature information will be used as the boundary conditions needed to solve the thermomechanical DDCP-FEM problem.

Acknowledgements

The authors thank the staff at the University of Louisville Rapid Prototyping Center for help with fabrication of test coupons. This research was supported by the National Institute of Standards and Technology (NIST), through a collaboration grant (number 70NANB12H262). NIST DMLS facilities were used to fabricate the mechanical test bars.

Reference:

- [1] Amato, K.N., Gaytan, S.M., Murr, L.E., Martinez, E., Shindo, P.W., Hernandez, J., Collins, S., and Medina, F. *Acta Materialia*, Volume 60(5), pp. 2229–2239.
- [2] Amato, K. N., Hernandez, J., Murr, L. E., Martinez, E., Gaytan, S.M., and Shindo, P.W. Comparison of Microstructures and Properties for a Ni-Base Superalloy (Alloy 625) Fabricated by Electron and Laser Beam Melting , *Journal of Materials Science Research*, Volume 1(2), pp. 3-41.
- [3] Shankar, V., Rao, Shankara, Mannan, S.L., ”Microstructure and Mechanical Properties of Inconel 625 Superalloy” *Journal of Nuclear Materials* 288 (2001) 222-223.
- [4] Metallography of Superalloys , G.F. Vander Voort, Buehler Ltd., October 2003 .
- [5] Metals Handbook Ninth Edition , Volume 9 , pp. 305 – 309 . ASM International , Materials Park, OH . 1985

- [6] Starr T.L., Rafi K., Stucker B., Scherzer C.M. (2012). “Controlling phase composition in selective laser melted stainless steels.” *Proceedings of 2012 Solid Freeform Fabrication Symposium*, the University of Texas, Austin.
- [7] Spierings, A. B., Schneider, M., & Eggenberger, R. (2011). Comparison of density measurement techniques for additive manufactured metallic parts. *Rapid Prototyping Journal*, 17(5), 380-386.
- [8] IN625 measured data by National Bureau of Standards.
- [9] Paul, C.P, Ganesh, P., Mishra, S.K., Bhargava, P., Negi, J., Nath, A.K., “Investigating laser rapid manufacturing for Inconel-625 components” *Journal of Optics & Laser Technology* 39 (2007) 800–805
- [10] Gibson, I., Rosen, D.W., and Stucker, B. Additive Manufacturing Technologies: Rapid Prototyping to Direct Digital Manufacturing. Springer, 2009.
- [11] Pal, D., Behera, S. and Ghosh, S. Crystal Plasticity Modeling of Creep and Microtwinning in Nickel based Superalloys, *United States National Congress on Computational Mechanics*, Columbus, OH, July 2009.
- [12] Pal, D. and Stucker, B.E. Dislocation Density Based Finite Element Modeling of Ultrasonic Consolidation, *Solid Freeform Fabrication Symposium Proceedings*, 2010, Austin, TX, August 2010.
- [13] Pal, D. and Stucker, B.E. Dislocation Density Based Finite Element Modeling of Ultrasonic Consolidation (**updated approach**), *Solid Freeform Fabrication Symposium Proceedings*, 2010, Austin, TX, August 2011.
- [14] Pal, D. Dislocation Density-Based Finite Element Method Modeling of Ultrasonic Consolidation (**update approach, detailed formulation**), PhD Thesis, Utah State University, August 2011.
- [15] Pal, D., and Stucker, B.E. Some Studies on Dislocation Density Based Finite Element Modeling of Ultrasonic Consolidation, *Proceedings of the 5th International conference on Virtual and Rapid Prototyping*, Leiria, Portugal, 2011.
- [16] Pal, D., and Stucker, B.E. Modeling of Ultrasonic Consolidation Using a Dislocation Density Based Finite Element Framework, *Virtual and Physical Prototyping Journal*, Volume 7(1), pp. 65-79.
- [17] Rodriguez , E., Medina, F., Espalin, D., Terrazas, C., Muse, D., Henry, C., MacDonald, E., Wicker, B. Rayan, “Integration of a Thermal Imaging Feedback Control System in Electron Beam Melting” *proceeding at The University of Texas at El Paso, El Paso, TX 79968, USA, 2012*

Notation:

* Represents the center of gravity of the distribution. Strongly influenced by coarse particles.

** Is calculated using the volume distribution data and is weighted to the small particles. This data is related to population

† The area mean is a type of "average" that is less weighted than mv by the presence of coarse particles and therefore shows smaller particle size. Mean dia. Represents a particle surface measurement.

†† Calculated CS does not reflect porosity or unique topographic characteristics of particles.